Controlling the electronic structure of $Co_{1-x}Fe_{2+x}O_4$ thin films through iron doping

J. A. Moyer,[1] C. A. F. Vaz,[1,*] E. Negusse,[2] D. A. Arena,[3] and V. E. Henrich[1]

[1]*Department of Applied Physics and Center for Research on Interface Structures and Phenomena, Yale University, New Haven, Connecticut 06511, USA*

[2]*Department of Physics, Montana State University, Bozeman, Montana 59717, USA*

[3]*National Synchrotron Light Source, Brookhaven National Laboratory, Upton, New York 11973, USA*

(Received 7 November 2010; published 19 January 2011)

The electronic, magnetic and transport properties of iron-doped cobalt ferrite ($Co_{1-x}Fe_{2+x}O_4$) thin films grown epitaxially on MgO (001) substrates are investigated by soft x-ray absorption and photoelectron spectroscopy, ultraviolet photoelectron spectroscopy, superconducting quantum interference device magnetometry, and resistivity measurements. The crystal structure for $Co_{1-x}Fe_{2+x}O_4$ is determined to be nearly inverse spinel, with the degree of inversion increasing for increased doping until it becomes fully inverse spinel for Fe_3O_4. The doped iron cations have a valency of 2+ and reside solely on octahedral sites, which allows for conduction owing to hopping between Fe^{2+} and Fe^{3+} octahedral cations. The addition of Fe^{2+} cations increases the electron density of states near the Fermi energy, shifting the Fermi level from 0.75 to 0 eV with respect to the top of the valence band, as the doping increases from $x = 0.01$ to 1. This change in electronic structure results in a change in resistivity by over two orders of magnitude. In contrast, the magnetic properties of $CoFe_2O_4$ thin films, characterized by a significantly reduced saturation magnetization compared to the bulk and large magnetic anisotropies, are affected less significantly by doping in the range from 0 to 0.63. These results show that $Co_{1-x}Fe_{2+x}O_4$ has tunable electronic properties while maintaining magnetic properties similar to $CoFe_2O_4$.

DOI: 10.1103/PhysRevB.83.035121 PACS number(s): 71.27.+a, 71.20.−b, 72.80.−r, 75.70.Ak

I. INTRODUCTION

The field of spintronics, which employs the electron spin along with the electron charge to design devices with novel functionalities, is the focus of much current research. Utilization of the spin degree of freedom provides opportunities to create devices with superior performance compared with those that use only electron charge.[1,2] Successes of spintronics include the use of magnetic tunnel junctions (MTJs) in read heads and magnetic random access memories (MRAMs), and the demonstration of electric-field control of ferromagnetism.[3–5] In order to advance to more complex spintronic devices, such as the spin field-effect transistor (SFET),[6] efficient spin injection into semiconductors is key. This requires the development of materials having both large spin polarizations at the Fermi level and a small conductivity mismatch with semiconductors.[2,7–9]

Complex ferri- or ferromagnetic metal oxides are one of the options in the search for efficient spin injection.[10] Complex oxides are well suited for the field of spintronics because of their highly correlated *d* electrons, which results in a wide variety of electronic and magnetic properties. They are also environmentally stable, and many have magnetic critical temperatures well above room temperature. One class of materials that has sparked renewed interest lately is the 3*d* transition-metal spinel ferrites, MFe_2O_4 ($M = 3d$ transition-metal cation). These materials have been predicted to have large spin polarizations,[11–15] but only magnetite ($M =$ Fe, Fe_3O_4) is electrically conducting in the bulk,[16,17] with a spin polarization measured to be as high as $-80\% \pm 5\%$ at the Fermi energy[18,19] (the negative sign indicates a net polarization of spin-down electrons).[20] The use of magnetite as an efficient spin injector has been limited by the ability to grow Fe_3O_4 on semiconductors, such as GaAs, with atomically abrupt interfaces[21–24] and by the large conductivity mismatch between Fe_3O_4 and semiconductors. The conductivity mismatch problem can be overcome by doping spinel ferrites with excess iron; this replaces M^{2+} cations with Fe^{2+} cations, creating new complex oxides of the form $M_{1-x}Fe_{2+x}O_4$, where x is the degree of doping. Recent work reported on $Mn_{1-x}Fe_{2+x}O_4$,[25,26] $Co_{1-x}Fe_{2+x}O_4$,[27] and $Zn_{1-x}Fe_{2+x}O_4$ (Refs. 26,28–30,) demonstrates that iron doping can change insulating spinel ferrites into conductors, with the conductivity controlled by the degree of doping. In addition, a thorough understanding of the electronic, transport, and magnetic properties is essential before attempting to synthesize spintronic devices with these materials. While the previous work on $Mn_{1-x}Fe_{2+x}O_4$ and $Zn_{1-x}Fe_{2+x}O_4$ covered a broad range of doping, the work on $Co_{1-x}Fe_{2+x}O_4$ was limited to $0.83 \leqslant x \leqslant 1$.[27]

In this study, we report detailed investigations of the structural, electronic, transport, and magnetic properties of molecular beam epitaxy (MBE)-grown $Co_{1-x}Fe_{2+x}O_4$ thin films over a wide doping range ($0.01 \leqslant x \leqslant 0.63$). We find that, with increasing Fe doping, the crystal structure changes from a nearly inverse spinel structure for $CoFe_2O_4$ to a fully inverse spinel structure for Fe_3O_4, showing that the iron that is added through doping takes the form of Fe^{2+}cations and resides solely on the octahedral sites. This allows for electron hopping between Fe^{2+} and Fe^{3+} cations on the octahedral sites, as confirmed by an increase in the density of states near the Fermi energy and by a marked decrease in resistivity with increasing doping. We find, however, that the effect of iron doping on the magnetic properties is less pronounced, leading to only a slight increase in the saturation magnetization. Our results show that the electronic and transport properties of doped $CoFe_2O_4$ can be tuned without strongly affecting the

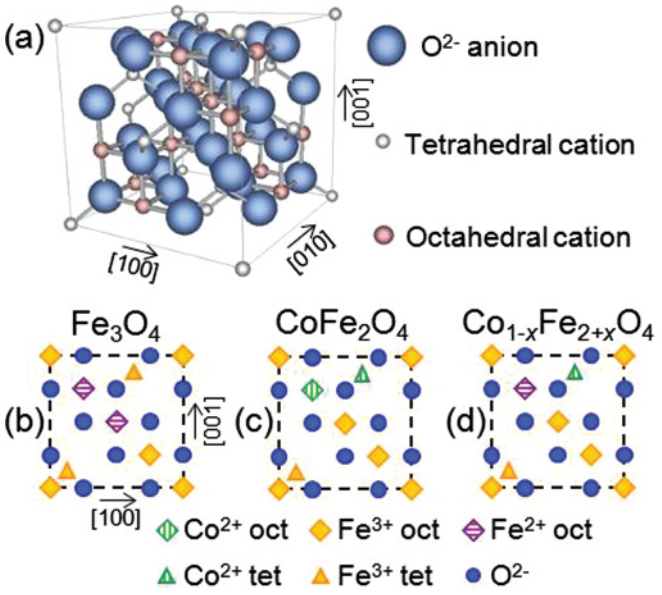

FIG. 1. (Color online) (a) Schematic of the spinel crystal structure, which is based on an oxygen fcc sublattice with the cations occupying interstitial sites: 1/3 of the cations located in 1/8 of the available tetrahedral sites and 2/3 of the cations located in 1/2 of the available octahedral sites. The octahedral and tetrahedral sites are antiferromagnetically aligned. (b)–(d) Schematic of the (010) crystal planes of (b) Fe_3O_4, (c) $CoFe_2O_4$, and (d) $Co_{1-x}Fe_{2+x}O_4$; the unit cells are designated by the dotted lines. The tetrahedral sites protrude from the (010) plane in the [010] direction by 1/8 of the lattice constant. Fe_3O_4 has the inverse spinel crystal structure, with all of the Fe^{2+} cations located on octahedral sites and the Fe^{3+} cations split evenly between the octahedral and tetrahedral sites. $CoFe_2O_4$ is primarily inverse spinel, with the majority of the Co^{2+} cations located on octahedral sites. $Co_{1-x}Fe_{2+x}O_4$ is similar to that of $CoFe_2O_4$ in that it is primarily inverse spinel with a majority of Co^{2+} cations located on octahedral sites, but with Fe^{2+} cations occupying only octahedral sites.

magnetic properties, thus offering improved control of properties for spin injection.

Because the stoichiometry of $Co_{1-x}Fe_{2+x}O_4$ falls between Fe_3O_4 and $CoFe_2O_4$ (cobalt ferrite), a knowledge of the electronic and crystal structure of the stoichiometric materials is helpful for understanding the off-stoichiometric, iron-doped $Co_{1-x}Fe_{2+x}O_4$. Magnetite has the cubic inverse spinel crystal structure [see Fig. 1(a)], with the tetrahedrally coordinated sites occupied by Fe^{3+} cations and the octahedrally coordinated sites occupied by an equal number of Fe^{2+} and Fe^{3+} cations [Fig. 1(b)]. At room temperature the Fe^{2+} and Fe^{3+} cations are located randomly on the octahedral sites. The sixth electron on Fe^{2+} cations is in a weakly bound t_{2g} state, and conductivity in magnetite occurs via electron hopping between Fe^{2+} and Fe^{3+} cations on the octahedral sites, with a hopping frequency on the order of 10^{11} Hz.[31] Below 120 K magnetite undergoes the so-called Verwey transition,[32] where the crystal structure changes from cubic to monoclinic, which is accompanied by an orbital and charge ordering and a drop in conductivity by over two orders of magnitude.[33–35] The tetrahedral and octahedral sites are antiferromagnetically coupled, resulting in a magnetic moment varying between 3.65 and 4.43 μ_B, depending on the theoretical model.[11,12,14,15,36] Hence, magnetite is a ferrimagnet, with a large critical temperature of $T_c = 858$ K.

Cobalt ferrite has a structure similar to magnetite, except that the Fe^{2+} cations are replaced by Co^{2+} cations. Because Co^{2+} is the preferred valence state for cobalt and Co^{2+} has no weakly bound electrons, the replacement of Fe^{2+} with Co^{2+} makes cobalt ferrite an insulator. The crystal structure of cobalt ferrite is no longer fully inverse spinel; the majority of Co^{2+} cations occupy octahedral sites, although a small fraction (2%–24%, depending strongly on the thermal history of the sample)[37] are located on the tetrahedral sites.[37,38] The Fe^{3+} cations are now distributed unevenly between the octahedral and tetrahedral sites [Fig. 1(c)]. Cobalt ferrite, like magnetite, is ferrimagnetic with a magnetic moment predicted by different theoretical models to be between 2.73 and 3 μ_B/f.u. for a perfect inverse spinel crystal structure;[11,12,15] the magnetic moment will increase with increased mixing of the Co^{2+} cations between the octahedral and tetrahedral sites. Cobalt ferrite has a large magnetic anisotropy owing to a spin-orbit stabilized doublet (with unquenched orbital momentum $l_z = +1$) ground state caused by a trigonal crystal field on the Co^{2+} octahedral cations,[27,39–45] with a cubic magnetocrystalline anisotropy constant, K_1, which is positive and larger by over an order of magnitude than the other 3d transition-metal spinel ferrites.[17,46] Thin films (~40–120 nm) grown on high symmetry substrates, such as MgO and $SrTiO_3$, show a reduced saturation magnetization of 25%–60% of bulk values.[43,46–48] The reduction of saturation magnetization in other ferrites has been attributed to antiphase boundaries,[49] which are created when crystal growth begins at different locations on the substrate, forming islands that are structurally out of phase with each other upon merging, giving rise to spin frustration at the boundaries. For ultrathin films (<7 nm), the saturation magnetization of cobalt ferrite increases above the bulk value because of increased mixing of the cations between the octahedral and tetrahedral sites.[47] It has a large magnetic critical temperature ($T_c = 793$ K) and is more environmentally stable than magnetite because Co^{2+} and Fe^{3+} are the most stable valence states of those cations, whereas Fe^{2+} cations easily oxidize to Fe^{3+}.[50]

When cobalt ferrite is doped with extra iron, $Co_{1-x}Fe_{2+x}O_4$, Fe^{2+} cations are expected to substitute for the Co^{2+} cations. With a reduced number of Co^{2+} cations, the crystal structure should be more nearly inverse spinel than the stoichiometric cobalt ferrite, because it is expected that the Fe^{2+} cations will reside solely on the octahedral sites [Fig. 1(d)]. It is known from previous work on powders and thin films that the addition of Fe^{2+} cations on the octahedral sites leads to electrical conduction owing to electron hopping between the Fe^{2+} and Fe^{3+} cations on those sites.[27,51] The amount of doping should permit control over the charge carrier density and allow for impedance matching between $Co_{1-x}Fe_{2+x}O_4$ films and a range of semiconductors.

II. EXPERIMENTAL DETAILS

Sample growth was carried out in a MBE growth chamber with a base pressure of 10^{-9} Torr. An analysis chamber,

with a base pressure of 10^{-10} Torr, is connected to the MBE growth chamber under UHV, which allows *in situ* analysis immediately following growth.[52] $Co_{1-x}Fe_{2+x}O_4$ thin films ($x = 0.01, 0.18, 0.39, 0.63, 1$) were grown epitaxially on square MgO (001) single-crystal substrates, chosen because of the small lattice mismatch of $\sim -0.3\%$ between the oxygen sublattices of MgO and $Co_{1-x}Fe_{2+x}O_4$, which produces a slight tensile strain in the $Co_{1-x}Fe_{2+x}O_4$ films. The MgO substrate was prepared by ultrasonic cleaning in acetone and methanol. The substrate was then rubbed on a polymide foam polishing pad wetted with methanol and loaded immediately into the growth chamber. Prior to growth, the substrate was annealed in an oxygen plasma using an electron cyclotron resonance (ECR) plasma source at an oxygen partial pressure of 2×10^{-5} Torr and a substrate temperature of 573 K. Iron contacts $\sim$17 nm thick were deposited onto the four corners of the substrate prior to film growth. When the $Co_{1-x}Fe_{2+x}O_4$ film was grown on top of the contacts, part of each contact remained uncovered; these contacts were used for the *ex situ* resistivity measurements and to electrically ground the sample for *in situ* photoelectron spectroscopy measurements.

The $Co_{1-x}Fe_{2+x}O_4$ films were grown by codeposition of metallic iron and cobalt, thermally evaporated from effusion cells, in a background of 3×10^{-7} Torr of molecular oxygen, with the MgO substrate held at 523 K (this growth temperature assures no diffusion of Mg ions into the films[44,53]). The growth rate was 0.2 nm/min and film thicknesses were $\sim$20 nm, determined using a calibrated quartz crystal thickness monitor and x-ray reflectivity. Different stoichiometries were obtained by adjusting the deposition rates of the cobalt and iron effusion cells while keeping the total deposition rate constant. Sample crystallinity was characterized *in situ* before and after growth with reflection high-energy electron diffraction (RHEED) and low-energy electron diffraction (LEED). The electronic structure was studied *in situ* with ultraviolet and x-ray photoelectron spectroscopies (UPS and XPS) using a double-pass cylindrical mirror energy analyzer (Φ 15-255G) with pass energies of 15 eV (0.24 eV energy resolution) and 25 eV (0.8 eV energy resolution, determined mostly from the x-ray source linewidth) for UPS and XPS, respectively. UPS spectra were obtained using a helium discharge tube and He II radiation ($h\nu = 40.8$ eV), while the XPS spectra were obtained using the Mg $K\alpha$ ($h\nu = 1253.6$ eV) and Al $K\alpha$ ($h\nu =$ 1486.6 eV) lines of a double-anode x-ray source. In order to minimize the overlap of Auger lines with the 2*p* XPS spectra, Mg $K\alpha$ and Al $K\alpha$ radiation were used to measure the Co 2*p* and Fe 2*p* XPS spectra, respectively.

After the *in situ* analysis, a 1-nm MgO capping layer was grown on top of the $Co_{1-x}Fe_{2+x}O_4$ films to protect the sample from oxidation for the *ex situ* measurements. Further structural characterization was carried out with x-ray diffraction and x-ray reflectivity (Cu $K\alpha$ line) using a Shidmazu diffractometer set in the parallel beam geometry. Magnetic measurements were made using a superconducting quantum interference device (SQUID) magnetometer (Quantum Design MPMS), while the sample resistivity was measured using the van der Pauw method[54] in a transport measurement system (Quantum Design PPMS). Soft x-ray absorption spectroscopy (XAS) was performed on beamline U4B at the National Synchrotron Light Source (NSLS) at Brookhaven National Laboratory [spectra measured in total electron yield (TEY) mode with energy resolutions of 0.42 eV for cobalt and 0.34 eV for iron]. All experiments were performed at room temperature except the SQUID and XAS measurements, which were performed at both 100 and 300 K.

III. RESULTS AND DISCUSSION

The crystal structure and surface quality were monitored during growth using RHEED (RHEED oscillations were not observed because of intensity fluctuations in the RHEED gun). The observation of sharp diffraction spots lying in a Laue arc and Kikuchi lines (not shown) confirms film epitaxy and shows that the surfaces are well ordered and nearly atomically flat. Spots were observed instead of streaks because of a large incidence angle between the electron beam and the sample. The results from RHEED are confirmed by LEED taken after film growth; representative results are shown in Fig. 2 for (a) an MgO (001) surface prior to growth, (b) a $Co_{0.61}Fe_{2.39}O_4$ film, and (c) an Fe_3O_4 film at an incident electron energy of 100 eV. The $Co_{0.61}Fe_{2.39}O_4$ LEED pattern is characteristic of the LEED patterns for all values of x except $x = 1$ (magnetite). The doubling of the periodicity of the $Co_{0.61}Fe_{2.39}O_4$ LEED pattern with respect to that of the MgO (001) surface demonstrates that the $Co_{1-x}Fe_{2+x}O_4$ films grow cube on cube on MgO (001) with a lattice constant twice that of MgO. The Fe_3O_4 LEED pattern shows a $\sqrt{2} \times \sqrt{2}R45^\circ$ reconstruction characteristic of an Fe_3O_4 surface that has not been oxidized to γ-Fe_2O_3.[53] The bright, sharp spots and the reconstruction of the Fe_3O_4 surface demonstrate that our films are nearly atomically flat and have the correct oxygen stoichiometry. X-ray diffraction measurements show only the MgO (002) and (004) planes; the $Co_{1-x}Fe_{2+x}O_4$ (004) and (008) planes cannot be distinguished from the MgO (002) and (004) planes because of the small lattice mismatch of -0.3% and thinness of the films. No other diffraction lines are present, confirming that the films are single phase. X-ray reflectivity confirms the sample thickness to be $\sim$20 nm.

XPS was used to determine the stoichiometry and cation valence states. Figure 3(a) shows the XPS Fe 2*p* spectra for samples with $x = 0.01$, 0.63, and 1. As x increases from 0.01 to 1, the $2p_{3/2}$ and $2p_{1/2}$ peaks shift to lower binding energies, and the satellite between the two peaks disappears. This is consistent with Fe^{2+} cations replacing Co^{2+} cations, which causes the XPS Fe 2*p* spectra to now contain contributions from both Fe^{2+} and Fe^{3+} cations. The 2*p* peaks for different iron cations do not occur at the same binding

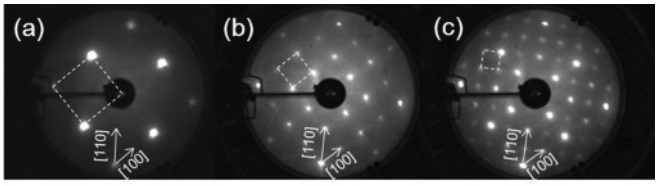

FIG. 2. LEED patterns for (a) MgO (001) substrate, (b) $Co_{0.61}Fe_{2.39}O_4$ film, and (c) Fe_3O_4 film for an incident electron energy of 100 eV. The reciprocal lattice unit cells are indicated by the boxes.

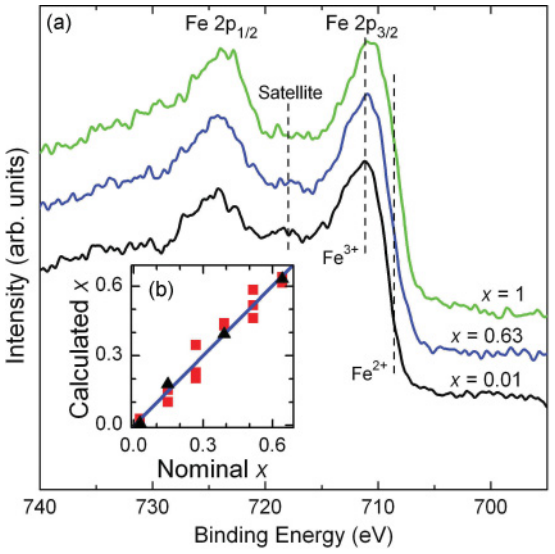

FIG. 3. (Color online) (a) Fe $2p$ XPS spectra of $Co_{0.99}Fe_{2.01}O_4$ ($x = 0.01$), $Co_{0.37}Fe_{2.63}O_4$ ($x = 0.63$), and Fe_3O_4 ($x = 1$). The binding energies of the $2p_{3/2}$ peaks for the Fe^{2+} and Fe^{3+} cations and the satellite for the Fe^{3+} cation are labeled. (b) Nominal stoichiometry vs calculated stoichiometry for 19 $Co_{1-x}Fe_{2+x}O_4$ films (red squares), overlaid with a linear least-squares fit. The black triangles are the calculated stoichiometries for the films discussed in this paper.

energy; the Fe^{2+} $2p_{3/2}$ peak has a binding energy ~2 eV lower than the Fe^{3+} $2p_{3/2}$ peak.[53,55] For $x > 0$, the $2p$ peaks contain contributions from both valence states, which results in a broadened peak that is shifted to a binding energy between those of the individual cations; this can be seen for the $2p_{3/2}$ peak in Fig. 3(a). Likewise, the Fe^{2+} cations have a characteristic satellite that occurs at a binding energy a few eV lower than the Fe^{3+} satellite. The presence of both satellites results in a roughly constant intensity between the $2p_{3/2}$ and $2p_{1/2}$ peaks, where neither satellite can be individually resolved, whereas for the $Co_{0.99}Fe_{2.01}O_4$ film, the satellite from the Fe^{3+} cations is clearly distinguishable. The peak locations and satellite intensities of our spectra match up well with the spectra presented by Chambers and Joyce, with our samples of $x = 0.01$, 0.63, and 1 corresponding to their samples of γ-Fe_2O_3 (Fe^{3+} only), partially oxidized Fe_3O_4 (small amount of Fe^{2+}), and Fe_3O_4 (large amount of Fe^{2+}), respectively.[53] The XPS data show that the $Co_{0.99}Fe_{2.01}O_4$ ($x = 0.01$) sample contains only Fe^{3+} cations; with increased doping, Fe^{2+} cations are added to the oxide. Co $2p$ XPS spectra (not shown) indicate only Co^{2+} cations for all stoichiometries.

To determine the stoichiometry of our samples from XPS core-level spectra, a Shirley background is subtracted from the Co $2p$, Fe $2p$, and O $1s$ spectra. The integrated intensities of the Co and Fe $2p$ spectra are then normalized by dividing by the integrated intensity of the O $1s$ spectrum, which is assumed to be the same for all x. Before calculating the stoichiometries, small oxygen and cobalt Auger lines included in the Co $2p$ and Fe $2p$ XPS spectra are subtracted. The normalized XPS intensities of the samples are then compared with XPS intensities from the known standards $CoFe_2O_4$ and $Fe3O_4$. Assuming that the intensity of the XPS signal changes linearly with the stoichiometry, we can determine the relative ratios of cobalt and iron to oxygen and calculate the amount of Co and Fe per formula unit by requiring that they add to three cations per formula unit. This procedure was used to determine the stoichiometry for 19 $Co_{1-x}Fe_{2+x}O_4$ films; the data of nominal stoichiometry versus calculated stoichiometry is shown graphically in Fig. 3(b). The black triangles correspond to the four $Co_{1-x}Fe_{2+x}O_4$ films discussed in this paper ($x = 1$ sample is not included in this figure), while the red squares correspond to 15 other sample growths. The data show a good correspondence between nominal and calculated stoichiometries with a standard deviation of 0.04; the calculated stoichiometries are the doping values quoted in this study.

In addition to XPS, which probes the occupied core-level density of states, we have carried out XAS measurements that probe both the empty valence-band density of states and the occupied core-level density of states. Analysis of XAS measurements allows for quantitative information to be gained about the site occupancies of the different cation valence states. The experimental Co XAS $L_{2,3}$ spectra for the four different $Co_{1-x}Fe_{2+x}O_4$ samples with $x < 1$ are displayed in Fig. 4(a). The total integrated intensity of each spectrum is normalized to show relative changes between peak heights. The L_3 edge is characterized by a sharp peak at the low energy end ($E = 777.75$ eV), whose amplitude and position are insensitive to doping; by two peaks, at ~779.25 and 780.25 eV, whose height and energy position vary with doping, both increasing with increasing x [shown in Fig. 4(b)] and by a shoulder at the high-energy end, which does not change significantly with doping. The L_2 edge, which is separated from the L_3 edge by an energy corresponding to the spin-orbit splitting of the $2p$ core levels, has less structure, where only one peak can be distinguished, whose amplitude increases slightly with iron doping. The corresponding Fe XAS $L_{2,3}$ spectra are displayed in Fig. 5(a); regions of interest are plotted in more detail in Figs. 5(c)–5(f) for the low-energy iron L_3 shoulder, low energy iron L_3 peak ($E = 708.5$ eV), the main iron L_3 peak ($E = 709.75$ eV), and the iron L_2 region, respectively. As x increases from 0.01 to 0.63, a low-energy shoulder develops on both the L_3 and L_2 peaks, along with an increase in the low-energy L_3 peak and a decrease in the main L_3 peak amplitude.

The experimental XAS spectra are compared to XAS spectra calculated using the Ligand field multiplet (LFM) model to determine the cationic origin of the different spectral features.[56,57] The LFM model calculates the spectra for a molecule complex, composed of a cation in a given ligand crystal field. By calculating the spectra of the relevant cationic states, the total LFM spectrum for the $Co_{1-x}Fe_{2+x}O_4$ thin film is obtained from a weighted linear superposition of the individual spectrum of each cation; this can then be compared with the measured XAS spetra. The individual spectra determine which cation state is responsible for each peak in the experimental spectrum, and the combination of the individual spectra gives quantitative information about the site occupancies of each cation state. LFM calculations were performed using the CTM4XAS 5.0 program[58] including full spin-orbit coupling, crystal-field effects, and reduction of the Slater integrals $F(dd)$, $F(pd)$, and $G(pd)$ to include

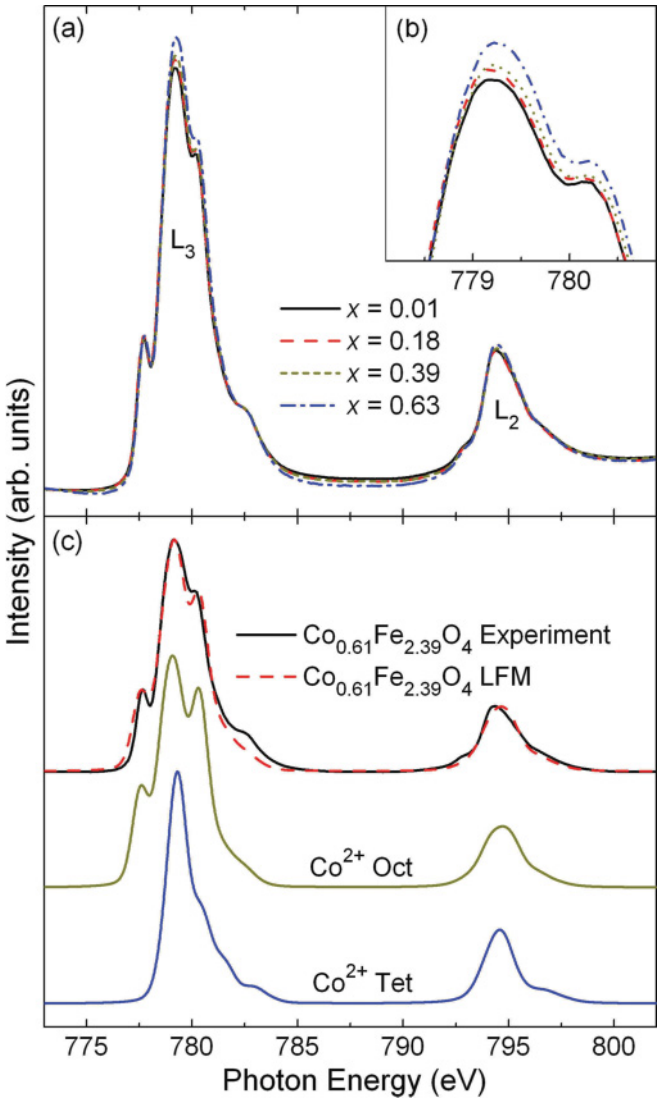

FIG. 4. (Color online) (a) Experimental Co $2p$ XAS spectra for four different $Co_{1-x}Fe_{2+x}O_4$ films, with $x = 0.01, 0.18, 0.39$, and 0.63. (b) Main L_3 peaks at 779.25 and 780.25 eV for the spectra in (a). (c) Comparison between the experimental Co $2p$ XAS spectrum and the calculated LFM spectra. The two spectra below are the individual LFM spectra for Co^{2+} octahedral cations and Co^{2+} tetrahedral cations. The total LFM spectrum is a linear combination of the two individual LFM spectra.

the interatomic configuration interaction.[59] The $F(dd)$, $F(pd)$, and $G(pd)$ integrals were reduced by 65%, 65%, and 68%, respectively, which is consistent to within ±15% with previous results on Fe_2O_3, Fe_3O_4, and $CoFe_2O_4$ thin films and synthetic crystals.[60–63] Quantitative estimates about the cation site occupancies were obtained by adjusting the site occupancies until the peak locations and heights matched the experimental data. All spectra are broadened by a Lorentzian with a half-width of 0.1 (0.3) eV for the L_3 (L_2) edge to account for core-hole lifetime broadening and by a Gaussian with a half-width of 0.34 eV to account for instrumental broadening.

Figure 4(c) shows the LFM calculations for the $L_{2,3}$ peaks of Co^{2+} octahedral and tetrahedral cations, as well as the experimental $Co_{0.61}Fe_{2.39}O_4$ spectrum overlaid with the

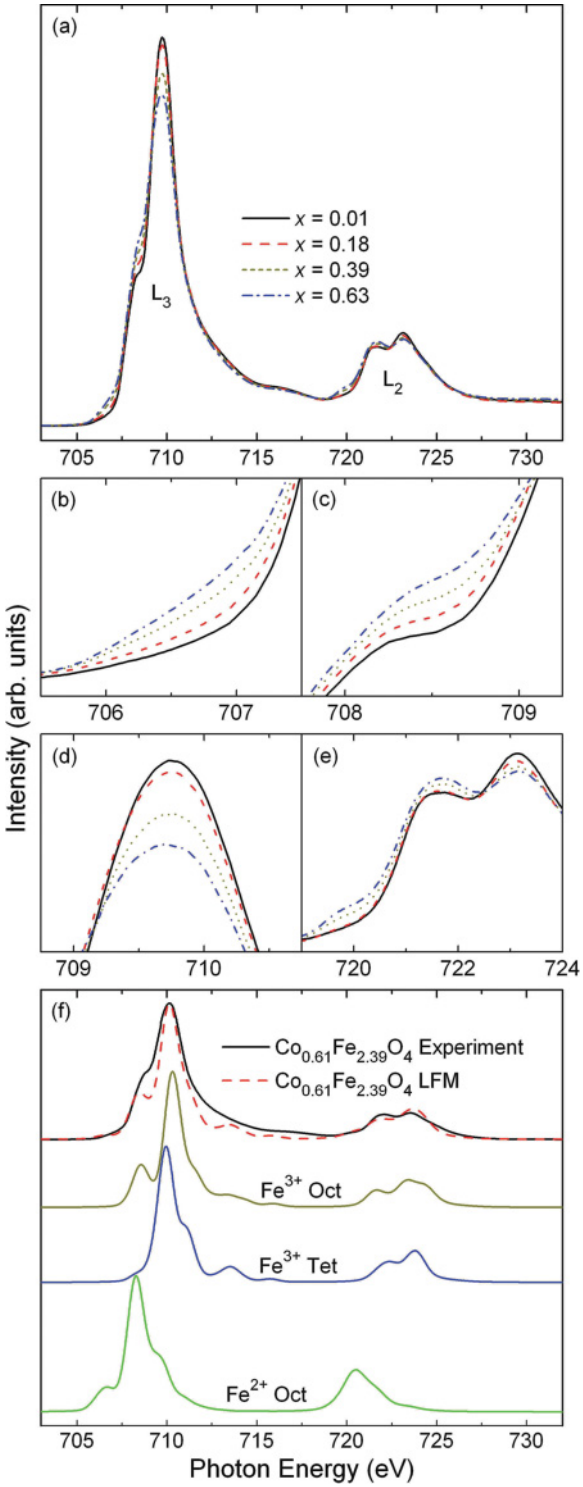

FIG. 5. (Color online) (a) Experimental Fe $2p$ XAS spectra for four different $Co_{1-x}Fe_{2+x}O4$ films, with $x = 0.01$, 0.18, 0.39, and 0.63. (b) Low-energy L_3 shoulder at 706.75 eV for the spectra in (a). (c) Low-energy L_3 peak at 708.5 eV for the spectra in (a). (d) Main L_3 peak at 709.75 eV for the spectra in (a). (e) Low-energy L_2 shoulder at 719.75 eV and L_2 peaks at 721.5 and 723.5 eV for the spectra in (a). (f) Comparison between the experimental Fe $2p$ XAS spectrum and the calculated LFM spectra. The three spectra below are the individual LFM spectra for Fe^{3+} octahedral cations, Fe^{3+} tetrahedral cations, and Fe^{2+} octahedral cations. The total LFM spectrum is a combination of the of the three individual LFM spectra.

respective LFM spectrum. The crystal-field strength used for the octahedral and tetrahedral cobalt cations is $10Dq = 1.2$ eV; this value matches well with the predicted value of ~1.2 eV for $Co_{1-x}Fe_{2+x}O_4$ octahedral cations[41] and the values of 1.2 and 0.9 eV used to describe the crystal fields of CoO (Ref. 64) and $CoFe_2O_4$.[62] The Co^{2+} octahedral cation has strong transition peaks that correspond to the three main L_3 peaks in the experimental spectrum, whereas the Co^{2+} tetrahedral cation has only one strong transition peak corresponding to the main L_3 peak. The tetrahedral cation also has many smaller transitions on the high-energy side of its L_3 peak that create a high-energy shoulder in the Co^{2+} tetrahedral spectrum, which adds intensity to the high-energy L_3 peak in the total LFM spectrum. Both the octahedral and tetrahedral cations contribute to the main L_3 peak, but their peaks occur at slightly different energies, resulting in an L_3 peak that is slightly broadened. The experimental L_2 peak is a single broadened peak that displays less structure. The calculated spectra for octahedral and tetrahedral Co^{2+} allow us to determine how the site occupancies of the cobalt cations change with stoichiometry. Because the Co^{2+} tetrahedral cations contribute only to the main and high-energy L_3 peaks, while the Co^{2+} octahedral cations contribute to all three peaks, the increasing heights of the main and high-energy L_3 peaks with increasing x show that the ratio between the tetrahedral and octahedral cations increases with increasing x. Because larger x values correspond to samples with more iron and less cobalt, this increase in the ratio between tetrahedral and octahedral cations shows that the iron is substituting more for the cobalt octahedral cations than for the tetrahedral cations.

The results of the calculations for the Fe^{3+} octahedral, Fe^{3+} tetrahedral, and Fe^{2+} octahedral cations at the $L_{2,3}$ edge are shown in Fig. 5(f), together with the experimental $Co_{0.61}Fe_{2.39}O_4$ spectrum overlaid with the corresponding LFM calculation. Crystal-field strengths used in the calculations for the octahedral and tetrahedral iron cations were $10Dq = 1.55$ and 0.6 eV, respectively, agreeing with previous studies on Fe_3O_4 and Fe_2O_3, which found crystal field values ranging from $10Dq = 1.2$ to 1.6 for octahedral cations and 0.6 eV for tetrahedral sites.[60,61,63] The Fe^{3+} octahedral cation has strong transitions that correspond to the low-energy L_3 and main L_3 peaks; the L_2 peak contains two peaks, which roughly correspond in energy to the two measured L_2 peaks. The spectrum for the Fe^{3+} tetrahedral cation is similar to that of the Fe^{3+} octahedral cation, except that it does not have any transitions corresponding to the low-energy L_3 peak. The L_2 peaks for the Fe^{3+} cations are different in shape, but correspond to roughly the same energies and have the same relative size. This results in the calculated L_2 LFM spectra being fairly insensitive to the Fe^{3+} octahedral-tetrahedral ratio. The Fe^{2+} octahedral cation has a strong transition peak that corresponds to the low-energy L_3 peak, a weak transition peak corresponding to the low-energy L_3 shoulder. and a single peak with less structure that corresponds to the low-energy L_2 shoulder. The presence of Fe^{2+} octahedral cations can clearly be seen in the L_3 and L_2 peaks by characteristic shoulders that have energies ~2 eV lower than the lowest Fe^{3+} peaks.

The comparison between the calculated and experimental spectra for the iron $L_{2,3}$ peaks is not as good as that for the cobalt $L_{2,3}$ peaks, but a great deal of information can still be gained by examining the energies of the calculated $L_{2,3}$ peaks of each of the individual cations. Comparing Fig. 5(f) with Figs. 5(a)–5(e) gives us a qualitative insight into how the cation valence states are changing with stoichiometry. The increase in the low-energy L_3 and L_2 shoulders and the low-energy L_3 peak with increasing x all occur because of larger amounts of Fe^{2+} octahedral cations, which have transitions occurring at energies corresponding to these three features. The decrease in the intensity of the main L_3 peak shows that the ratio of Fe^{3+} cations to the total number of iron cations is decreasing with increasing x, because this peak is solely comprised of Fe^{3+} cations. This shows that, as x increases, iron is being added to the samples in the form of Fe^{2+} octahedral cations, replacing the Co^{2+} octahedral cations. These results agree with the Co $L_{2,3}$ XAS and Fe $2p$ XPS analysis.

By comparing the data with the LFM calculations, we can obtain quantitative estimates for the preferred cation site locations; we primarily consider the Co edge, for which the LFM calculations provide better agreement. The results are displayed in Fig. 6, which shows the number of cations per formula unit versus x for the four samples with $x < 1$. The four data points for each cation are fit by a second degree polynomial that is extended out to $x = 1$ to give a guide to the eye; the fact that the fits extrapolate to the correct values for $x = 1$ (magnetite) suggests that such a dependence is a good description of the data over the whole doping range. One finds that, as x increases, Fe^{2+} cations substitute for Co^{2+} cations on the octahedral sites, confirming our qualitative observations. The number of Co^{2+} tetrahedral cations is also slowly decreasing with increasing x. These cobalt cations are not replaced directly by Fe^{2+} cations; instead they are

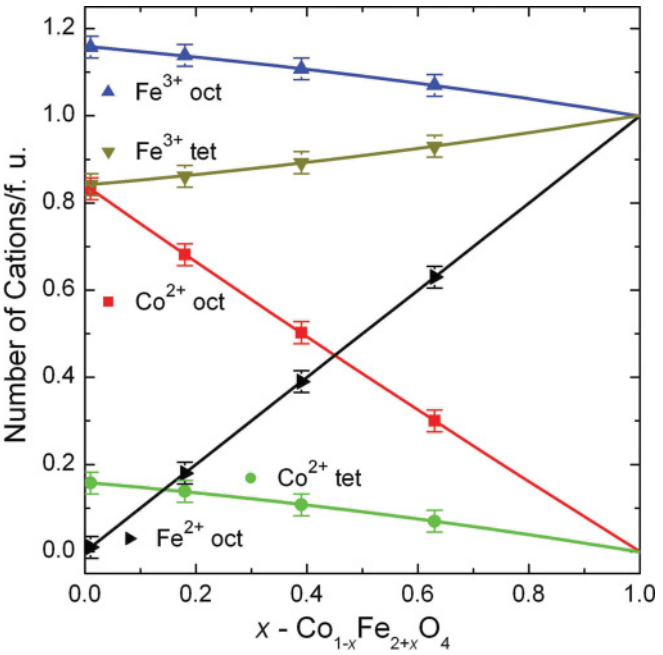

FIG. 6. (Color online) Variation in the number of each cation per formula unit (f.u.) determined by XAS vs sample stoichiometry. The error bars are estimated from the comparison of the total LFM calculated spectra with the experimental spectra. The data points are fit to second degree polynomials.

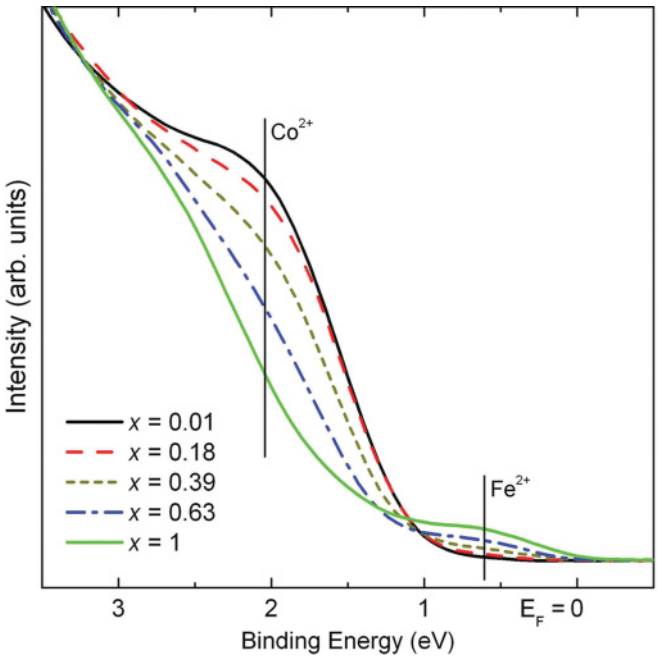

FIG. 7. (Color online) UPS spectra for five different $Co_{1-x}Fe_{2+x}O_4$ samples with $0.01 \leqslant x \leqslant 1$.

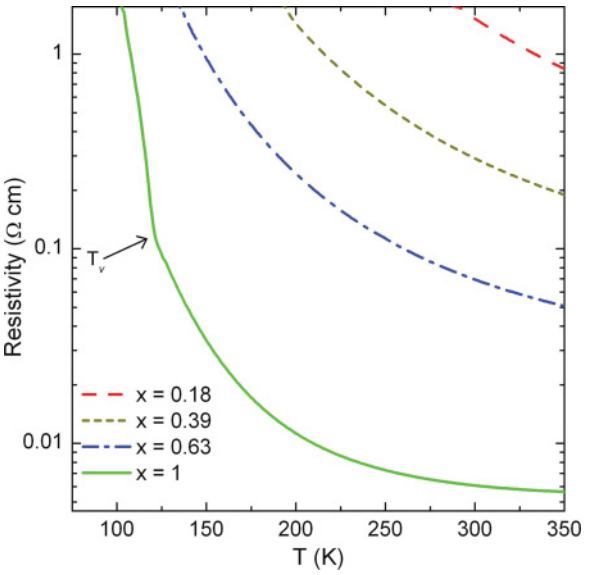

FIG. 8. (Color online) Resistivity vs temperature measurements for the samples with $0.18 \leqslant x \leqslant 1$.

replaced by Fe^{3+} cations, with the Fe^{2+} cations occupying the octahedral sites. The extrapolation of the data shows that the Fe^{3+} octahedral, Fe^{3+} tetrahedral, and Fe^{2+} octahedral cations tend toward a value of 1 at $x = 1$, while the Co^{2+} octahedral and tetrahedral cations are tending toward a value of 0, which corresponds to a fully inverse spinel crystal structure for Fe_3O_4, as expected. This quantitative analysis demonstrates that, as the doping increases, the crystal structure is becoming more nearly inverse spinel, with the Fe^{2+} cations residing solely on the octahedral sites, which is necessary for conduction via hopping between the Fe^{2+} and Fe^{3+} octahedral cations.

UPS measurements complement the information gained from XPS and XAS measurements by probing a different part of the electronic structure, the occupied valence-band states. Figure 7 displays the UPS spectra for the five different compositions with $0.01 \leqslant x \leqslant 1$. This graph shows the valence-band spectra from 3.5 eV below the Fermi energy up to the Fermi energy ($E_F = 0$). Within this energy range, there are many spectral features that change with increased iron doping (i.e., peak shapes, position of peak centroids, etc.); even with these changes, a simplified, rigid band-structure model can be used to demonstrate how iron doping directly changes the band structure, causing an increase in conductivity. Comparison of the UPS spectra with published valence-band spectra and band-structure calculations of $CoFe_2O_4$ (Ref. 11) and Fe_3O_4 (Refs. 11,14,65, and 66) allows us to identify the cationic origin of the states in this region. At approximately a binding energy of 2 eV, there is a band of states corresponding to the Co^{2+} cations, while the states at ~0.6 eV correspond to the Fe^{2+} t_{2g} states. As x increases, the spectral intensity at ~2 eV decreases, while the intensity at 0.6 eV slowly increases owing to the decreased number of Co^{2+} cations and the increase in Fe^{2+} cations. The increase in Fe^{2+} t_{2g} states results in a significant change in the position of the Fermi energy level with respect to the top of the valence band. For $Co_{0.99}Fe_{2.01}O_4$, this difference is ~0.75 eV, but it decreases for increasing x and eventually disappears for Fe_3O_4. The increase in the density of states near the Fermi energy, and the change in position of the Fermi energy with respect to the valence band, demonstrates that, through iron doping, the band structure near the Fermi energy can be controlled in a systematic way.

The effect of iron doping on the electrical resistivity of $Co_{1-x}Fe_{2+x}O_4$ is shown in Fig. 8. These measurements confirm that our tailoring of the band structure leads directly to significant changes in the conductivity of our samples. The measurements show that varying the doping level between $0.18 \leqslant x \leqslant 1$ changes the resistivity of the samples by over two orders of magnitude at room temperature. As the temperature decreases, the resistivities of all the $Co_{1-x}Fe_{2+x}O_4$ samples with $x < 1$ increase at approximately the same rate, whereas the resistivity of the Fe_3O_4 sample increases at a slower rate. At temperatures below room temperature, the change in resistivity with doping increases to over three orders of magnitude. At lower temperatures, the resistivity of the Fe_3O_4 sample begins to increase more rapidly, and at 120 K the Verwey transition becomes clearly visible, which is characteristic of Fe_3O_4 films that have not been oxidized to γ-Fe_2O_3,[32] confirming that the Fe_3O_4 sample has the correct oxygen stoichiometry.

It is clear from the above that doping cobalt ferrite with excess iron causes a change in the electronic band structure near the Fermi energy that leads directly to a change in the resistivity of the samples. The effect of doping on the magnetic properties of the samples is determined by measuring the magnetic response of the system. Figure 9 shows in-plane *M-H* loops for five samples with $0.01 \leqslant x \leqslant 1$ at both 100 K [Fig. 9(a)] and 300 K [Fig. 9(b)] with the magnetic field aligned along the [010] direction. A diamagnetic substrate contribution, similar for all samples, was removed from the data. At 100 K, the Fe_3O_4 ($x = 1$) film has a saturation magnetization of

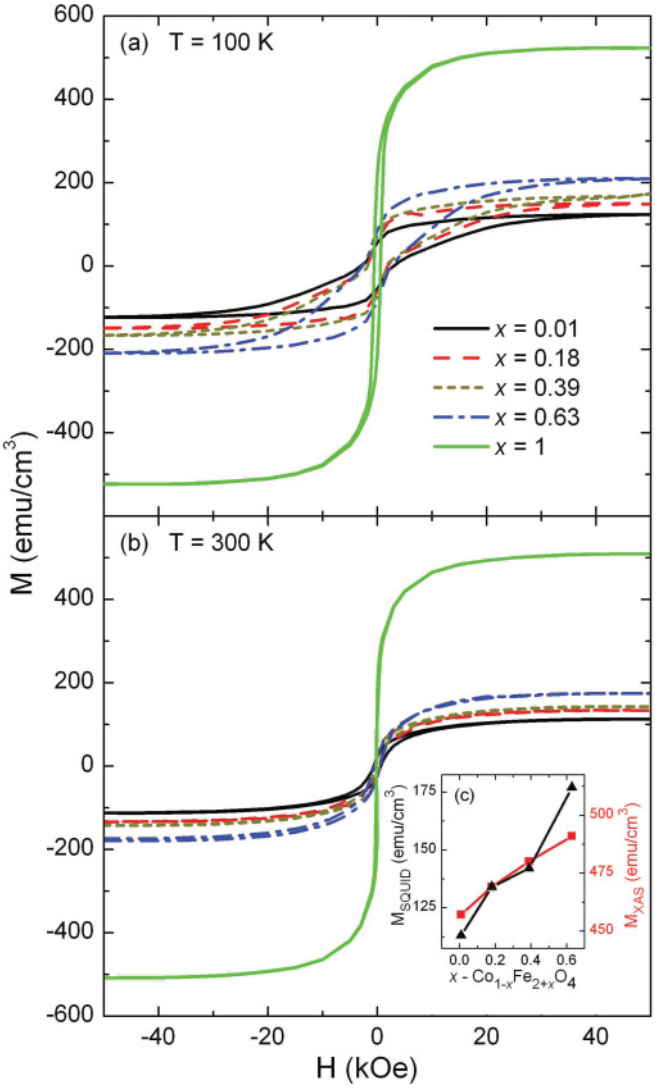

FIG. 9. (Color online) In-plane *M-H* loops of $Co_{1-x}Fe_{2+x}O_4$ samples with $0.01 \leqslant x \leqslant 1$ at (a) 100 K and (b) 300 K with the magnetic field aligned along the [010] direction. (c) Comparison of saturation magnetic moments at 300 K measured by SQUID magnetometry (black triangles) and predicted spin magnetic moment from XAS analysis (red squares) vs sample stoichiometry.

524 emu/cm^3, which is consistent with theoretical values, which vary between 480 and 582 emu/cm^3.[11,12,14,15,36] However, $Co_{1-x}Fe_{2+x}O_4$ films have saturation magnetizations that are drastically reduced from their bulk values; the measured saturation magnetization of the $Co_{0.99}Fe_{2.01}O_4$ ($x = 0.01$) sample is 123 emu/cm^3 compared with the theoretical values, which vary between 359 and 394 emu/cm^3.[11,12,15] This reduction in magnetization has been reported in $CoFe_2O_4$ thin films grown on MgO and $SrTiO_3$.[43,46–48] Figures 9(a) and 9(b) show that the reduced magnetization occurs not just for the stoichiometric sample, but also for all of the doped $Co_{1-x}Fe_{2+x}O_4$ samples at both 100 and 300K. Figure 9(c) graphically displays the variation of the saturation magnetization with iron doping at 300 K. For comparison, the predicted spin magnetic moment for each sample, as determined by the site occupancies from the XAS measurements, is also plotted. The measured magnetic moment increases with roughly the same slope as the predicted magnetic moments. It has been suggested that reduced magnetizations in ferrite films occur because of the presence of antiphase boundaries.[49] If this were the case, however, we should expect a similar reduced magnetization for the Fe_3O_4 sample as well. Hence, because this reduced magnetization occurs only for the samples that contain Co^{2+} cations, regardless of the amount of Co^{2+}, we conclude that the presence of Co^{2+} cations must play a significant role in suppressing the saturation magnetization. The coercive fields for the $Co_{1-x}Fe_{2+x}O_4$ samples at 100 K are all approximately $H_c \sim 2.5$ kOe, which is much larger than $H_c = 575$ Oe for the Fe_3O_4 sample. The remnant magnetization is ~43% of the saturation magnetization for both the $Co_{1-x}Fe_{2+x}O_4$ samples and the Fe_3O_4 sample. The *M-H* loops taken at 300 K have slightly different characteristics than the loops taken at 100 K. The saturation magnetization of the Fe_3O_4 sample is ~95% of the value at 100 K, while the saturation magnetization of the $Co_{1-x}Fe_{2+x}O_4$ samples dropped to ~75% of the value at 100 K, which suggests a reduced critical temperature for the $Co_{1-x}Fe_{2+x}O_4$ films. Overall, the magnetometry data show that, while the transport properties of the $Co_{1-x}Fe_{2+x}O_4$ thin films are altered dramatically through Fe doping, the magnetic properties of $Co_{1-x}Fe_{2+x}O_4$ change less markedly up to $x = 0.63$.

From the results presented above, a detailed understanding of how iron doping affects the electronic structure of $Co_{1-x}Fe_{2+x}O_4$ emerges. Stoichiometric $CoFe_2O_4$ has a crystal structure that is nearly inverse spinel, with the majority of Co^{2+} cations residing on octahedral sites. These cations give rise to valence-band states that are ~0.75 eV below the Fermi energy. When $CoFe_2O_4$ is doped with iron, Fe^{2+} cations replace the Co^{2+} cations on the octahedral sites only. The crystal structure becomes more nearly inverse spinel and tends toward a fully inverse spinel structure for Fe_3O_4. The Fe^{2+} cations give rise to new valence-band states near the Fermi energy, which shifts the Fermi energy with respect to the top of the valence band. For doping of $x = 1$, a finite density of states at the Fermi energy develops. The location of the Fe^{2+} cations on octahedral sites is important because conduction occurs via electron hopping between Fe^{2+} and Fe^{3+} cations only. This change in electronic structure is observed directly in a resistivity change of over two orders of magnitude for doping levels ranging from $x = 0.18$ and 1.

The magnetic properties of $Co_{1-x}Fe_{2+x}O_4$ do not behave in the same way as the electronic and structural properties. Unlike the electronic and structural properties, which change smoothly from $CoFe_2O_4$ to Fe_3O_4 as the samples are doped with more iron, the unique magnetic properties of $CoFe_2O_4$ do not change over a large doping range (up to at least $x = 0.63$); magnetically, the films continue to behave as stoichiometric $CoFe_2O_4$. Even though the amount of Co^{2+} is reduced with iron doping, the films continue to display large anisotropies as predicted,[39,41] and the reduced magnetic moment roughly changes with doping as is expected from site occupancy information gained from XAS.

IV. CONCLUSIONS

In summary, we have grown epitaxial $Co_{1-x}Fe_{2+x}O_4$ thin films with $0.01 \leqslant x \leqslant 1$ using oxide MBE. These films are

structurally well ordered and nearly atomically flat, with the Fe_3O_4 sample exhibiting a $\sqrt{2} \times \sqrt{2}R45^\circ$ surface reconstruction and a Verwey transition, which confirms the correct oxygen stoichiometry for our films. Core-level spectroscopies examined the site location and valence states for the cobalt and iron cations, while ultraviolet photoelectron spectroscopy probed the occupied valence band near the Fermi energy. These measurements showed that the electronic structure can be tailored to yield controllable changes in the resistivity of more than two orders of magnitude. Magnetometry results showed that, even though the electronic structure changes significantly because of the presence of Fe^{2+} cations on octahedral sites, only a slight change in the saturation magnetization occurs. The ability to tailor the band structure without affecting the magnetic properties makes $Co_{1-x}Fe_{2+x}O_4$ a promising material for future spintronics applications and warrants future studies to determine the degree of spin polarization at the Fermi level and the potential of $Co_{1-x}Fe_{2+x}O_4$ as a spin injector.

ACKNOWLEDGMENTS

The authors acknowledge Jason Hoffman for his help with the transport measurements and financial support by the NSF through Grant No. MRSEC DMR 0520495 (CRISP). One of us (E.N.) acknowledges the support of the Army Research Office under Grant No. W911NF-08-1-0325 and DOE under Grant No. DE-08NT0004115. Use of the National Synchrotron Light Source, Brookhaven National Laboratory, was supported by the U.S. Department of Energy, Office of Science, Office of Basic Energy Sciences, under Contract No. DE-AC02-98CH10886.

*Present address: Paul Scherrer Institut, 5232 Villigen PSI, Switzerland.

[1] S. A. Wolf, D. D. Awschalom, R. A. Buhrman, J. M. Daughton, S. von Molnar, M. L. Roukes, A. Y. Chtchelkanova, and D. M. Treger, Science **294**, 1488 (2001).
[2] I. Zutic, J. Fabian, and S. Das Sarma, Rev. Mod. Phys. **76**, 323 (2004).
[3] H. Ohno, D. Chiba, F. Matsukura, T. Omiya, E. Abe, T. Dietl, Y. Ohno, and K. Ohtani, Nature (London) **408**, 944 (2000).
[4] H. J. A. Molegraaf, J. Hoffman, C. A. F. Vaz, S. Gariglio, D. van der Marel, C. H. Ahn, and J. M. Triscone, Adv. Mater. (Weinheim, Ger.) **21**, 3470 (2009).
[5] C. A. F. Vaz, J. Hoffman, Y. Segal, J. W. Reiner, R. D. Grober, Z. Zhang, C. H. Ahn, and F. J. Walker, Phys. Rev. Lett. **104**, 127202 (2010).
[6] S. Datta and B. Das, Appl. Phys. Lett. **56**, 665 (1990).
[7] G. Schmidt, D. Ferrand, L. W. Molenkamp, A. T. Filip, and B. J. van Wees, Phys. Rev. B **62**, R4790 (2000).
[8] M. Johnson and J. Byers, Phys. Rev. B **67**, 125112 (2003).
[9] E. I. Rashba, Phys. Rev. B **62**, R16267 (2000).
[10] J. M. D. Coey and C. L. Chien, MRS Bull. **28**, 720 (2003).
[11] Z. Szotek, W. M. Temmerman, D. Kodderitzsch, A. Svane, L. Petit, and H. Winter, Phys. Rev. B **74**, 174431 (2006).
[12] V. N. Antonov, B. N. Harmon, and A. N. Yaresko, Phys. Rev. B **67**, 024417 (2003).
[13] H.-T. Jeng and G. Y. Guo, J. Magn. Magn. Mater. **239**, 88 (2002).
[14] Z. Zhang and S. Satpathy, Phys. Rev. B **44**, 13319 (1991).
[15] M. Penicaud, B. Siberchicot, C. B. Sommers, and J. Kubler, J. Magn. Magn. Mater. **103**, 212 (1992).
[16] C. D. Owens, Proc. IRE **44**, 1234 (1956).
[17] E. P. Wohlfarth, *Ferromagnetic Materials: A Handbook on the Properties of Magnetically Ordered Substances* (North-Holland, Amsterdam, 1980).
[18] Y. S. Dedkov, U. Rudiger, and G. Guntherodt, Phys. Rev. B **65**, 064417 (2002).
[19] M. Fonin, Y. S. Dedkov, R. Pentcheva, U. Rudiger, and G. Guntherodt, J. Phys. Condens. Matter **19**, 315217 (2007).
[20] C. A. F. Vaz, C. H. Ahn, and V. E. Henrich, in *Epitaxial Ferromagnetic Films and Spintronic Applications*, edited by A. Hirohata and Y. Otani (Research Signpost, Kerala, India, 2009), p. 145.
[21] Y. X. Lu, J. S. Claydon, E. Ahmad, Y. B. Xu, M. Ali, B. J. Hickey, S. M. Thompson, J. A. D. Matthew, and K. Wilson, J. Appl. Phys. **97**, 10C313 (2005).
[22] Y. X. Lu, J. S. Claydon, E. Ahmad, Y. B. Xu, S. M. Thompson, K. Wilson, and G. van der Laan, IEEE Trans. Magn. **41**, 2808 (2005).
[23] M. Paul, A. Muller, A. Ruff, B. Schmid, G. Berner, M. Mertin, M. Sing, and R. Claessen, Phys. Rev. B **79**, 233101 (2009).
[24] E. J. Preisler, J. Brooke, N. C. Oldham, and T. C. McGill, J. Vac. Sci. Technol. B **21**, 1745 (2003).
[25] J.-S. Kang, G. Kim, H. J. Lee, D. H. Kim, H. S. Kim, J. H. Shim, S. Lee, Hangil Lee, J.-Y. Kim, B. H. Kim, and B. I. Min, Phys. Rev. B **77**, 035121 (2008).
[26] J. Takaobushi *et al.*, Phys. Rev. B **76**, 205108 (2007).
[27] D. Tripathy, A. O. Adeyeye, C. B. Boothroyd, and S. N. Piramanayagam, J. Appl. Phys. **101**, 013904 (2007).
[28] J. Takaobushi *et al.*, Appl. Phys. Lett. **89**, 242507 (2006).
[29] S. Ueda *et al.*, Appl. Phys. Express **1**, 077003 (2008).
[30] D. Venkateshvaran, M. Althammer, A. Nielsen, S. Geprägs, M. S. Ramachandra Rao, S. T. B. Goennenwein, M. Opel, and R. Gross, Phys. Rev. B **79**, 134405 (2009).
[31] B. Balko and G. R. Hoy, Physica B **86**, 953 (1977).
[32] E. J. W. Verwey, Nature (London) **144**, 327 (1939).
[33] M. Iizumi, T. F. Koetzle, G. Shirane, S. Chikazumi, M. Matsui, and S. Todo, Acta Crystallogr. Sect. B **38**, 2121 (1982).
[34] D. Schrupp *et al.*, Europhys. Lett. **70**, 789 (2005).
[35] P. W. Anderson, Phys. Rev. **102**, 1008 (1956).
[36] D. J. Huang, C. F. Chang, H.-T. Jeng, G. Y. Guo, H.-J. Lin, W. B. Wu, H. C. Ku, A. Fujimori, Y. Takahashi, and C. T. Chen, Phys. Rev. Lett. **93**, 077204 (2004).
[37] G. Hu, J. H. Choi, C. B. Eom, V. G. Harris, and Y. Suzuki, Phys. Rev. B **62**, R779 (2000).
[38] G. A. Sawatzky, F. van der Woude, and A. H. Morrish, Phys. Rev. **187**, 747 (1969).
[39] M. Tachiki, Prog. Theor. Phys. **23**, 1055 (1960).
[40] J. C. Slonczewski, J. Appl. Phys. **29**, 448 (1958).
[41] J. C. Slonczewski, Phys. Rev. **110**, 1341 (1958).
[42] G. F. Dionne, *Magnetic Oxides* (Springer, Boston, 2009).
[43] S. A. Chambers, R. F. C. Farrow, S. Maat, M. F. Toney, L. Folks, J. G. Catalano, T. P. Trainor, and G. E. Brown Jr., J. Magn. Magn. Mater. **246**, 124 (2002).

[44]L. Horng, G. Chern, M. C. Chen, P. C. Kang, and D. S. Lee, J. Magn. Magn. Mater. **270**, 389 (2004).
[45]R. V. Chopdekar and Y. Suzuki, Appl. Phys. Lett. **89**, 182506 (2006).
[46]Y. Suzuki, G. Hu, R. B. van Dover, and R. J. Cava, J. Magn. Magn. Mater. **191**, 1 (1999).
[47]F. Rigato, J. Geshev, V. Skumryev, and J. Fontcuberta, J. Appl. Phys. **106**, 113924 (2009).
[48]G. Hu, V. G. Harris, and Y. Suzuki, IEEE Trans. Magn. **37**, 2347 (2001).
[49]D. T. Margulies, F. T. Parker, M. L. Rudee, F. E. Spada, J. N. Chapman, P. R. Aitchison, and A. E. Berkowitz, Phys. Rev. Lett. **79**, 5162 (1997).
[50]V. E. Henrich and P. A. Cox, *The Surface Science of Metal Oxides* (Cambridge University Press, Cambridge, 1994).
[51]G. H. Jonker, J. Phys. Chem. Solids **9**, 165 (1959).
[52]H.-Q. Wang, E. I. Altman, and V. E. Henrich, Phys. Rev. B **77**, 085313 (2008).
[53]S. A. Chambers and S. A. Joyce, Surf. Sci. **420**, 111 (1999).
[54]L. J. van der Pauw, Philips Res. Rep. **13**, 1 (1958).
[55]C. D. Wagner, W. M. Riggs, L. E. Davis, G. E. Moulder, and G. E. Muilenberg, *Handbook of X-ray Photoelectron Spectroscopy* (Perkin-Elmer, Eden Praire, MN, 1979).
[56]F. M. F. de Groot, J. C. Fuggle, B. T. Thole, and G. A. Sawatzky, Phys. Rev. B **42**, 5459 (1990).
[57]G. van der Laan and I. W. Kirkman, J. Phys. Condens. Matter. **4**, 4189 (1992).
[58]E. Stavitski and F. M. F. de Groot, Micron **41**, 687 (2010).
[59]R. D. Cowan, *The Theory of Atomic Structure and Spectra* (University of California Press, Berkeley, 1981).
[60]P. Kuiper, B. G. Searle, P. Rudolf, L. H. Tjeng, and C. T. Chen, Phys. Rev. Lett. **70**, 1549 (1993).
[61]P. Kuiper, B. G. Searle, L.-C. Duda, R. M. Wolf, and P. J. van der Zaag, J. Electron Spectrosc. Relat. Phenom. **86**, 107 (1997).
[62]G. van der Laan, E. Arenholz, R. V. Chopdekar, and Y. Suzuki, Phys. Rev. B **77**, 064407 (2008).
[63]E. Arenholz, G. van der Laan, R. V. Chopdekar, and Y. Suzuki, Phys. Rev. B **74**, 094407 (2006).
[64]S. Imada and T. Jo, J. Magn. Magn. Mater. **104**, 2001 (1992).
[65]V. I. Anisimov, I. S. Elfimov, N. Hamada, and K. Terakura, Phys. Rev. B **54**, 4387 (1996).
[66]R. J. Lad and V. E. Henrich, Phys. Rev. B **39**, 13478 (1989).